Unsteady Flamelet Modeling of Differential Diffusion in Turbulent Jet Diffusion Flames

HEINZ PITSCH*

Center for Energy and Combustion Research, Department of Applied Mechanics and Engineering Sciences, 563 EBU II, 9500 Gilman Drive, University of California San Diego, MC 0411, La Jolla, CA 92093-0411, USA

An unsteady flamelet model, which will be called the Lagrangian Flamelet Model, has been applied to a steady, turbulent $CH_4/H_2/N_2$–air diffusion flame. The results have been shown to be in reasonable agreement with experimental data for axial velocity, mixture fraction, species mass fractions, and temperature. The application of three different chemical mechanisms leads to the promising conclusion that the state-of-the-art mechanisms yield almost identical results. To explain the still remaining differences from the experimental data, the effects of differential diffusion are discussed. Three possible mechanisms leading to differential diffusion are proposed: Firstly, the occurrence of a laminar mixing layer in a region very close to the nozzle exit; secondly, the molecular diffusivity being of the same order of magnitude as the turbulent eddy diffusivity; thirdly, a typical length scale of the mixing layer thickness being smaller than the small turbulent eddies leading to a laminar sublayer. By investigating the computational results for the considered configuration, the first mechanism has been concluded to be the only possibility. Further calculations have been performed, which account for differential diffusion by assuming the flow to be laminar very close to the nozzle and switching to unity Lewis numbers downstream of the potential core. The results lead to a significant improvement of the agreement to experimental data. It can be shown from the computational results and the experimental data that the differential diffusion effects arise from this laminar region. However, even though the Lewis numbers are assumed to be unity throughout the remaining part of the flow field these differential diffusion effects remain to a certain extent, even in the far downstream region, affecting for instance the centerline temperature by approximately 100 K. This demonstrates that differential diffusion can cause a strong history effect in turbulent jet diffusion flames.   © 2000 by The Combustion Institute

INTRODUCTION

Unsteady flamelet modeling of steady turbulent diffusion flames has been demonstrated to yield good predictions for temperature and the concentrations of chemical components including OH and NO in the numerical simulation of a nitrogen diluted H_2/air jet diffusion flame [1]. In this study it has also been shown that it is important to account for unsteady effects, if slow physical processes, such as radiation, or slow chemical processes, such as the formation of nitric oxides, are considered. In particular, unsteady effects appear if the time of flight of a fluid particle is shorter than the time needed to achieve a steady-state solution.

The model presented in Ref. 1 relies on the assumption of unity Lewis numbers for the chemical species. However, it has been shown in many experimental studies that effects of nonunity Lewis numbers can be observed close to the nozzle in low Reynolds number [2–4] as well as in high Reynolds number [3, 5, 6] turbulent

diffusion flames. Drake et al. [2, 4] obtained from experiments in turbulent H_2/air diffusion flames, differential diffusion effects in the concentration profiles of H_2 and N_2, decreasing with axial distance from the nozzle and with increasing Reynolds number. Meier et al. [6] investigated nitrogen diluted, nonpremixed H_2/air flames and found strong nonequal diffusion effects by comparison of O-atom and H-atom based mixture fraction definitions accompanied by noticeable superequilibrium temperatures. Because of the small Lewis number of the hydrogen molecule, nonequal diffusion effects are more pronounced in hydrogen flames, especially in the case of diluted fuel. However, also in hydrocarbon flames, where the Lewis numbers of most of the involved chemical species are close to unity, the appearance of differential diffusion has been clearly demonstrated, for instance, by Bergmann et al. [5] and Barlow and Frank [3]. Support for these findings has also been given by the results of direct numerical simulation (DNS) calculations [7–10].

Some authors have already suggested modeling approaches in the frame of different com-

---

*Corresponding author. E-mail: hpitsch@ames.ucsd.edu

bustion models. Bilger [11], for instance, suggested a model, which by perturbation about the equal diffusion case provided effective element diffusion coefficients. In a recent modeling study based on the conditional moment closure (CMC) combustion model, Nilsen and Kosály [10] suggested an empirical relation as a closure model of a term in the CMC equations, which represents differential diffusion effects. Both studies use DNS data to validate the proposed expression. Chen and Chang [12] developed a closure to incorporate differential diffusion effects in various mixing models to be used in probability density function (pdf) transport combustion models.

The aim of this study is the numerical modeling of a turbulent $CH_4/H_2/N_2$–air jet diffusion flame using an unsteady flamelet model and the comparison of the results with experimental data. In addition, the effects of differential diffusion in turbulent nonpremixed flames and the transition to equal diffusion for heat and matter will be investigated, and a model will be proposed that is substantially different from previous suggestions.

MATHEMATICAL MODEL

Flow Field Solution

The diffusion flame configuration used in this study has been experimentally investigated by Bergmann et al. [5] and Hassel et al. [13]. The fuel stream consists of 22.1% CH_4, 33.2% H_2, and 44.7% N_2 in volumetric parts and is introduced into the flow field through a nozzle with a diameter of $D = 8$ mm and a mean velocity of 42.15 m/s. This leads to a fuel exit Reynolds number of Re = 15,200. The stoichiometric mixture fraction is $Z_{st} = 0.167$. A surrounding nozzle with a diameter of 140 mm supplies air with an exit velocity of 0.3 m/s. The radial velocity distribution of the fuel is assumed to obey the 1/7 power law.

The solution of the flow field is obtained by using the FLUENT code. The original code has been extended by the solution of the turbulent mean and the variance of the mixture fraction. The energy equation is solved in the form of an enthalpy equation, where the enthalpy is defined to include the heat of formation of the chemical species, such that the transport equation has no chemical source term. The applied turbulence model is a standard $\bar{k} - \bar{\epsilon}$ model that includes buoyancy effects and a correction for round jets as proposed by Pope [14]. The calculations have been performed in axisymmetric coordinates for a 1000×400 mm axial $\times$ radial domain using a 191×77 cell nonequidistant grid.

Lagrangian Flamelet Model

The unsteady flamelet model applied in this study has been described in detail in Ref. 1. Therefore, only a brief survey and some details, which are not given in Ref. 1 will be provided here.

The flamelet model for nonpremixed combustion is a conserved scalar approach. The scalar used to characterize the local mixture of fuel and oxidizer is the mixture fraction Z, which is according to Ref. 15, for a two-feed system defined by the solution of the conservation equation

$$\rho \frac{\partial Z}{\partial t} + \rho \mathbf{v} \cdot \nabla Z - \nabla \cdot (\rho D_Z \nabla Z) = 0 \qquad (1)$$

with the boundary conditions of $Z = 1$ in the fuel stream and $Z = 0$ in the oxidizer stream. D_Z is the mixture fraction diffusivity, which is defined as

$$D_Z = \frac{\lambda}{\rho c_p}, \qquad (2)$$

where λ is the heat diffusivity, ρ the density, and c_p the specific heat capacity at constant pressure. The mixture fraction definition given by Eqs. 1 and 2 corresponds in the case of equal Lewis numbers for all chemical species to an element mixture fraction based definition as, for example, given by Masri and Bilger [16], where the Lewis number of species i is defined as

$$Le_i = \frac{\lambda}{\rho D_i c_p} \qquad (3)$$

and D_i is the molecular diffusivity of species i.

Equations for the turbulent mean of the mixture fraction $\tilde{Z}$ and its variance $\widetilde{Z''^2}$ are

calculated for the whole flow field, where the tilde denotes Favre averaging. Using a presumed pdf for the mixture fraction Z, whose shape depends on the local values of $\tilde{Z}$ and $\widetilde{Z''^2}$, the turbulent mean values of the species mass fractions $\tilde{Y}_i$ can be determined provided that a unique relationship among the species mass fractions and the mixture fraction is known.

In flamelet modeling, this relation is given by the solution of the flamelet equations, which have been given by Peters [17, 18] for unity Lewis numbers of the chemical species as

$$\rho \frac{\partial Y_i}{\partial t} - \rho \frac{\chi}{2} \frac{\partial^2 Y_i}{\partial Z^2} - \dot{m}_i = 0 \tag{4}$$

$$\rho \frac{\partial T}{\partial t} - \rho \frac{\chi}{2} \left(\frac{\partial^2 T}{\partial Z^2} + \frac{1}{c_p} \frac{\partial c_p}{\partial Z} \frac{\partial T}{\partial Z} + \frac{\partial T}{\partial Z} \sum_{k=1}^{N} \right.$$

$$\left. \cdot \left(1 - \frac{c_{pk}}{c_p} \right) \frac{\partial Y_k}{\partial Z} \right) + \frac{1}{c_p} \left(\sum_{k=1}^{N} h_k \dot{m}_k + \dot{q}_R''' \right) \right)$$

$$= 0. \tag{5}$$

Here, t denotes the time, T the temperature, χ the scalar dissipation rate, $\dot{q}_R'''$ the rate of radiative heat loss per unit volume, and N is the number of chemical species. h_k, c_{pk}, and $\dot{m}_k$ are the enthalpy, the specific heat capacity at constant pressure, and the chemical production rate per unit volume of species k, respectively.

The scalar dissipation rate, appearing in Eqs. 4 and 5 is defined as

$$\chi = 2D_Z (\nabla Z)^2 \tag{6}$$

and accounts for the influence of the flow field on the flame structure.

It has been mentioned earlier that it is important to describe the transient behavior of the flamelet if slow processes are involved. In the unsteady flamelet model described here, the flamelets are therefore allowed to undergo changes while they are convectively transported through the considered flow configuration. The flamelets are assumed to be introduced in the flow field at the nozzle exit. From there they travel downstream with the axial velocity at stoichiometric mixture. Hence, the axial position x of the flamelet is uniquely related to the time of flight t as

$$t = \int_0^x \frac{1}{u(x')|(\tilde{Z} = Z_{\mathrm{st}})} \, dx'. \tag{7}$$

This approach corresponds to a Lagrangian treatment of the flamelet development and will therefore be called the Lagrangian Flamelet Model in the following to distinguish it from unsteady flamelet models applied to unsteady flow situations as, for instance, in Refs. 19 and 20. In this study one representative flamelet is solved simultaneously and coupled with the flow field calculation.

The mixture fraction dependence of the scalar dissipation rate needed for the solution of the flamelet equations is modeled following Ref. 1 as

$$\chi = \chi_{\mathrm{st}} f(Z), \tag{8}$$

with

$$f(Z) = \frac{Z^2}{Z_{\mathrm{st}}^2} \frac{\ln Z}{\ln Z_{\mathrm{st}}}. \tag{9}$$

Nilsen and Kosály [10] have shown from DNS of decaying turbulence in an initially nonpremixed system that a function similar to Eq. 9 provides a good estimate for the mixture fraction dependence of the scalar dissipation rate. To accomplish a closure of the problem, the temporal development of the scalar dissipation rate has to be obtained from the flow field solution. Equation 8 shows that χ depends only on its stoichiometric value and the mixture fraction and also that χ_{st} and Z are statistically independent. Then, the turbulent mean of the scalar dissipation rate can be written as

$$\tilde{\chi} = \int_{\chi_{\mathrm{st}}} \chi_{\mathrm{st}}' \tilde{P}(\chi_{\mathrm{st}}') \, d\chi_{\mathrm{st}}' \int_Z f(Z') \tilde{P}(Z') \, dZ', \tag{10}$$

where $\tilde{P}$ denotes the Favre averaged pdf. In Eq. 10 the first integral defines the mean scalar dissipation rate conditioned on Z_{st} as

$$\langle \chi_{\mathrm{st}} \rangle = \int_{\chi_{\mathrm{st}}} \chi_{\mathrm{st}}' \tilde{P}(\chi_{\mathrm{st}}') \, d\chi_{\mathrm{st}}'. \tag{11}$$

If $\tilde{\chi}$ is expressed in terms of the $\bar{k} - \tilde{\epsilon}$ turbulence model as [21]

$$\tilde{\chi} = c_\chi \frac{\tilde{\epsilon}}{\tilde{k}} \widetilde{Z''^2}, \tag{12}$$

with Eq. 10, the mean scalar dissipation rate conditioned on stoichiometric mixture becomes

$$\langle \chi_{\text{st}} \rangle = \frac{c_\chi \frac{\tilde{\epsilon}}{\tilde{k}} \widetilde{Z''^2}}{\displaystyle\int_0^1 \frac{Z^2}{Z_{\text{st}}^2} \frac{\ln Z}{\ln Z_{\text{st}}} \tilde{P}(Z) \, dZ}. \tag{13}$$

The flamelet equations are solved using Eq. 8 with

$$\chi_{\text{st}} \equiv \langle \widehat{\chi_{\text{st}}} \rangle, \tag{14}$$

where $\langle \widehat{\chi_{\text{st}}} \rangle$ is the average of $\langle \chi_{\text{st}} \rangle$ over a particular volume V. Note that because the closure of the flamelet equations has been achieved by using the conditional averaged scalar dissipation rate, the results of the solution of the flamelet equations are also assumed to be conditionally averaged quantities.

Since $\langle \chi_{\text{st}} \rangle$ is a quantity conditioned on stoichiometric mixture, the volume average is determined by weighting $\langle \chi_{\text{st}} \rangle$ with the instantaneous area of stoichiometric mixture enclosed by the volume

$$\langle \widehat{\chi_{\text{st}}} \rangle = \frac{\displaystyle\int_A \overline{\langle \chi_{\text{st}} \rangle \, dA'}}{\displaystyle\int_A dA'}. \tag{15}$$

Considering the volume V, it can be shown [22] that the integral of a positive function $f(\mathbf{x}, t)$ over the volume, weighted with the absolute value $|\nabla \varphi(\mathbf{x}, t)|$ of a scalar field $\varphi(\mathbf{x}, t)$, is equal to the sum of the surface integrals of the function $f(\mathbf{x}, t)$ over all isosurfaces $\psi = \varphi(\mathbf{x}, t)$. This has been expressed by Kollmann and Chen [23] as

$$\int_V f(\mathbf{x}, t) |\nabla \varphi(\mathbf{x}, t)| \, dV' = \int_0^1 \int_{A_\varphi(\psi)} f(\mathbf{x}, t) \, dA' \, d\psi. \tag{16}$$

If the mixture fraction $Z(\mathbf{x}, t)$ is chosen for the scalar field function $\varphi(\mathbf{x}, t)$ and the fine grained pdf $\delta[Z_{\text{st}} - Z(\mathbf{x}, t)]$ as the function $f(\mathbf{x}, t)$, the

surface of stoichiometric mixture can be expressed as a function of the enclosing volume

$$\int_V \delta(Z_{\text{st}} - Z) |\nabla Z(\mathbf{x}, t)| \, dV' = A_{Z_{\text{st}}} \tag{17}$$

and in the limit $dV \to 0$

$$dA_{\text{st}} = |\nabla Z(\mathbf{x}, t)| \delta(Z_{\text{st}} - Z(\mathbf{x}, t)) \, dV. \tag{18}$$

The pdf of a function ϕ can be defined by the ensemble average of the fine grained pdf as [24]

$$\bar{P}(\phi') = \overline{\delta(\phi - \phi(\mathbf{x}, t))}. \tag{19}$$

Introducing Eq. 18 into Eq. 15 and calculating $(|\nabla Z| | Z = Z_{\text{st}})$ from the definition of the scalar dissipation rate Eq. 6 as

$$(|\nabla Z| | Z = Z_{\text{st}}) = \sqrt{\frac{\langle \chi_{\text{st}} \rangle}{2D}}, \tag{20}$$

the use of Eq. 19 leads to

$$\langle \widehat{\chi_{\text{st}}} \rangle = \frac{\displaystyle\int_V \langle \chi_{\text{st}} \rangle^{3/2} \bar{\rho} \bar{P}(Z_{\text{st}}) \, dV'}{\displaystyle\int_V \langle \chi_{\text{st}} \rangle^{1/2} \bar{\rho} \bar{P}(Z_{\text{st}}) \, dV'}. \tag{21}$$

In the particular case considered here, $\langle \widehat{\chi_{\text{st}}} \rangle$ should denote a radial average and the integration is performed in the limit $dx \to 0$. In a numerical simulation dx corresponds to the axial spacing of the computational mesh. The radial average of the scalar dissipation rate conditioned on stoichiometric mixture is shown in Fig. 1 as a function of the nozzle distance. The maximum value close to the nozzle is approximately $\langle \widehat{\chi_{\text{st}}} \rangle = 140 \text{ s}^{-1}$ and then decreases strongly with increasing nozzle distance. At the point of the maximum centerline temperature, which is at approximately $x/D = 60$, the scalar dissipation rate has already dropped to a value of $\langle \widehat{\chi_{\text{st}}} \rangle \approx 0.6 \text{ s}^{-1}$.

In Fig. 2 a comparison of different approximations of the scalar dissipation rate is shown for a radial slice at $x/D = 10$. The solid line is the unconditional turbulent mean scalar dissipation rate as determined by Eq. 12, the dashed line has been calculated with Eq. 8 with the values of χ_{st} at each point determined from Eq.
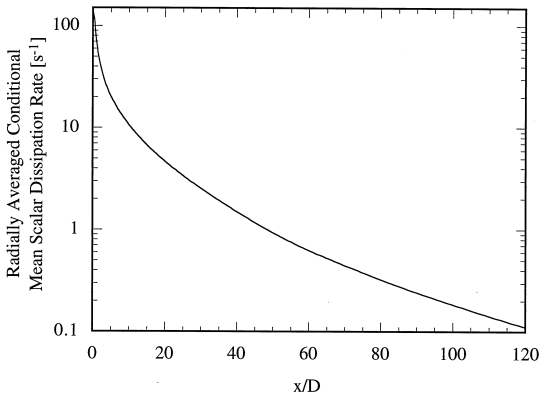
Fig. 1. Radially averaged scalar dissipation rate conditioned on stoichiometric mixture as a function of nozzle distance (Eq. 21).

13, and the dotted line is Eq. 8 with χ_{st} from Eq. 21, which is the model used in the solution of the flamelet equations. All approximations yield quite similar results for small values of the mixture fraction, but in the very rich part the approximations deviate from each other. The unconditional mean is lower than the conditional mean scalar dissipation rate because of the ensemble averaging. Actually, the radial average (dotted line) should be equal to the conditional mean scalar dissipation rate (dashed line). The lower values indicate that one particular flamelet does not extend in the radial direction. The radial average of the scalar dissipation rate in conjunction with Eq. 8 reconstructs the actual flamelet, whereas the other two approximations represent the values of a radial slice. However, it has been shown in Ref. 15 that the impact of differences in the scalar dissipation rate in the rich part is quite weak.
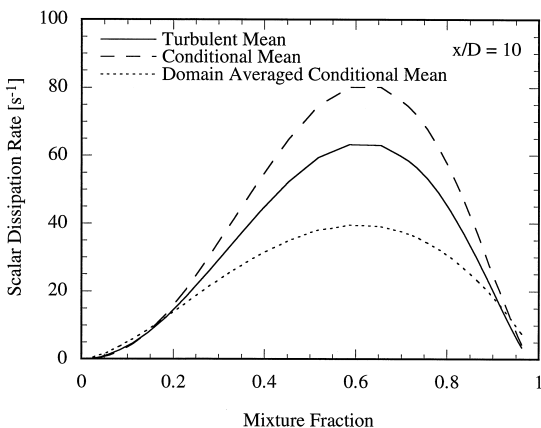
For the unsteady flamelet calculations, a reduced 20-step mechanism has been used. Based on the chemical mechanism given by Warnatz et al. [25] consisting of 295 elementary reactions among 34 chemical species, steady-state assumptions have been introduced for some radicals. The results obtained by using the reduced mechanism show essentially no differences from calculations employing the detailed reaction scheme.

Differential Diffusion

The Lagrangian Flamelet Model presented in the previous section relies on the assumption of unity Lewis numbers. In the following the possibility of extending the model to account for nonequal Lewis numbers will be discussed.

It has been mentioned in the introductory discussion that differential diffusion effects appear mainly very close to the nozzle and vanish for high Reynolds numbers. The impact on flames in practical applications is therefore negligible in most cases, although in flow situations slightly above the transition Reynolds number, differential diffusion is more important than in the diffusion flame investigated in the present paper. As mentioned earlier, this configuration has been investigated experimentally by Bergmann et al. [5], and differential diffusion effects have been reported to be very pronounced within a range extending from the nozzle to approximately $x/D = 10$.

In this section, three possible mechanisms, which would allow differential diffusion in turbulent flames are discussed and the individual importance for the investigated flame will be determined. It will be concluded in the following that the first of these, the laminar near field flow, is the predominant mechanism responsible for differential diffusion in the investigated flame. Although the remaining two mechanisms will be shown to be not important here, they should be discussed as possible alternatives in different flow situations.

Fig. 2. Comparison of turbulent mean scalar dissipation rate (Eq. 12), conditional mean scalar dissipation rate (Eqs. 8 and 13), and radially averaged conditional mean scalar dissipation rate (Eqs. 8 and 21) at $x/D = 10$ as a function of the mixture fraction.

Laminar Near Field Flow

It has been concluded from many studies that the near field of jet diffusion flames might exhibit laminar structures within the mixing layer, which would certainly make molecular diffusion the dominant transport contribution within the mixing layer [5, 26–30].

Yule et al. [26] found from the investigation of transitional jets that diffusion flames have a laminarizing effect and an enlarged potential core when compared with nonreacting jets.

Schefer et al. [27] investigated the temporal development of turbulence–chemistry interactions in the near field of methane diffusion flames at a moderate jet-exit Reynolds number of Re = 7000. The obtained laser-induced fluorescence (LIF) intensities of CH and CH_4 revealed laminar flame structures enveloping semi-organized, large-scale vortical structures. Similar results have also been found by Chen et al. [28] in propane jet diffusion flames with high Reynolds numbers up to Re $\approx$ 15,000. In addition, it has been found from the analytic analysis of vorticity generation and destruction that buoyancy and volumetric expansion lead to a suppression of the vorticity in the fuel-rich regime, which could explain the laminarization of the near field region of jet diffusion flames.

Clemens and Paul [29] studied reacting and nonreacting nonpremixed jets. They also found the near field consisting of a laminar region around the reaction zone and organized vortical structures in the inner core. The laminarization of the mixing layer and the separation of the vortical region from the reaction zone has sometimes been attributed to the lowering of the Reynolds number caused by the increased viscosity due to the high temperature in the reaction zone. However, by comparison of reactive and nonreactive jets, it is shown in Ref. 29 that the strong density gradients, in flames caused by the heat release, are dominant in reducing the shear layer thickness and extending the potential core.

In a numerical study of flow–chemistry interactions in the near field of nonpremixed jets, Soteriou [30] concluded that the initial separation of the high vorticity region and the reaction zone is amplified by combustion-induced volumetric expansion. Interestingly, it has been
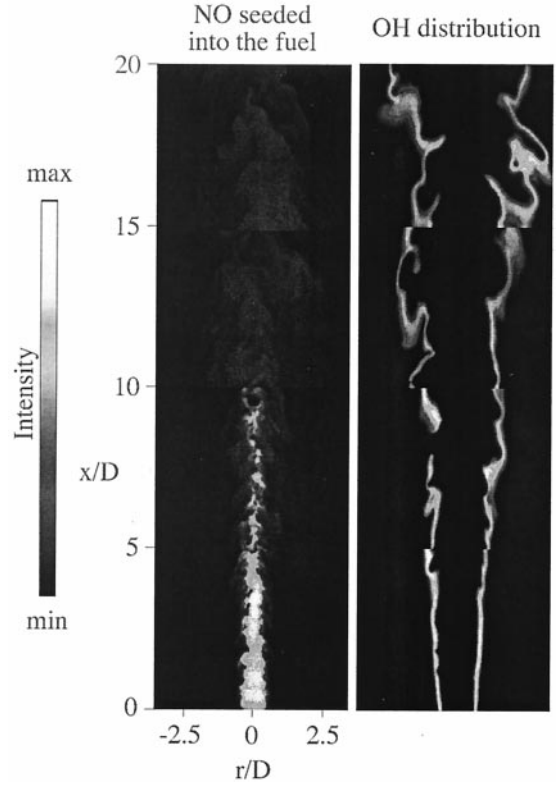

Fig. 3. LIF intensity of NO seeded into fuel and LIF intensity of OH in $CH_4/H_2/N_2$–air jet diffusion flame obtained by Bergmann et al. [5].

found that the maximum vorticity can often be located within the potential core, outside the region of mixture fraction variation.

Hence, there is experimental, analytic, and numerical evidence that even in high Reynolds number flows in the near field of jet diffusion flames there exists a turbulent potential core surrounded by a laminar mixing layer, which includes the reaction zone. It is obvious that this region is governed by molecular diffusion and will be affected by nonunity Lewis numbers. Figure 3 shows experimentally obtained results by Bergmann et al. reproduced from Ref. 5 for the $CH_4/H_2/N_2$ flame investigated in the present paper. The left frame shows fluorescence intensity of NO seeded into the fuel. The bright regions represent the pure fuel forming the potential core, which extends to approximately 5 to 10 nozzle diameters downstream. Large-scale vortical structures can be obtained at the edges of the core which are formed in the shear layer between the fuel and the surrounding

oxidizer. The OH fluorescence signal, given in the right frame of Fig. 3, indicates that the reaction zone is still within a laminar environment separated from the vortical region. Interactions among the turbulence-generating shear layer and the region around the reaction zone start at about $x/D = 5$, still exhibiting almost unwrinkled layers until $x/D = 10$. The differential diffusion effects, which have been clearly demonstrated to occur in this flame, are explained in Ref. 5 by the absence of turbulence within the mixing layer in regions close to the nozzle. These effects are pronounced at $x/D = 5$, and although turbulence develops in the mixing layer thereafter, the effects of differential diffusion remain even far downstream as will be shown later in this paper.

Molecular Diffusivity

A second and very obvious possibility to allow molecular diffusion effects emerging in turbulent flows is that the value of the molecular diffusivity D_i of a particular species i is in the same order of magnitude as the turbulent diffusivity D_t. Note that this argument actually includes the above discussed situation of a laminar flow region. However, the argument of a laminar mixing layer in the near field of the nozzle is treated separately, because of the complete absence of turbulence in this particular situation.

Because the molecular diffusivities of the individual components can be considerably different, these can be related to the mixture fraction diffusivity by using the Lewis number and Eq. 2 as

$$D_i = \frac{D_Z}{\text{Le}_i}. \tag{22}$$

The Lewis numbers of most species are close to unity. However, for the hydrogen radical, for instance, the Lewis number is $\text{Le}_H \approx 0.2$. The turbulent diffusivity can be related to the eddy viscosity ν_t by the turbulent Schmidt number

$$\text{Sc}_t = \frac{\nu_t}{D_t}, \tag{23}$$

which is assumed to be close to unity. In the frame of the $\tilde{k} - \tilde{\epsilon}$ model the turbulent eddy viscosity ν_t can be expressed as
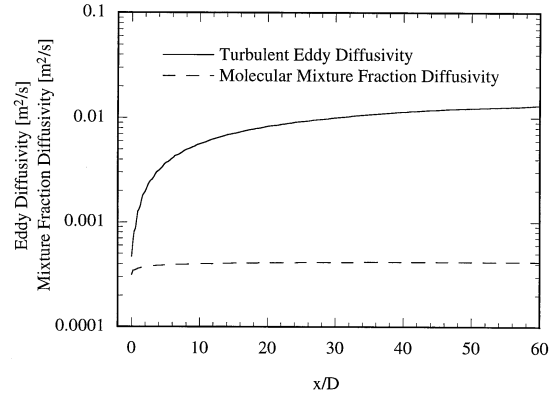

Fig. 4. Comparison of turbulent eddy diffusivity and mixture fraction diffusivity along the contour of stoichiometric mixture.

$$\nu_t = C_D \frac{\tilde{k}^2}{\tilde{\epsilon}} \tag{24}$$

with $C_D = 0.09$. For a simple comparison of molecular and turbulent diffusivity of the chemical components, the mixture fraction diffusivity can then be compared to the turbulent eddy diffusivity calculated from Eqs. 23 and 24.

It is well known that in fully developed turbulence, the turbulent eddy viscosity is usually much larger than the molecular quantities. This is demonstrated in Fig. 4 for the diffusion flame under investigation, where the turbulent eddy diffusivity conditioned on stoichiometric mixture is compared to the molecular mixture fraction diffusivity conditioned on stoichiometric mixture. The molecular diffusivity and the turbulent eddy diffusivity are of comparable magnitude close to the nozzle. The eddy diffusivity rises then within the first five nozzle diameters of axial distance to a value one order of magnitude larger than the molecular diffusivity, which remains almost constant. Hence, even for the hydrogen radical, which has the highest molecular diffusivity, the turbulent diffusivity becomes larger within the first five nozzle diameters. The considered flame has a Reynolds number of Re = 15,000, which is clearly above transition, so that this conclusion could change for lower Reynolds numbers.

Scale Separation

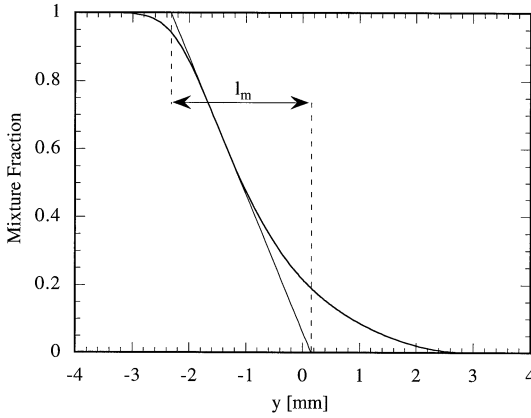The third possible explanation is the separation of the small scales of the turbulence and the

Fig. 5. Definition of the mixing layer thickness l_m.

mixing layer width. In the case that the characteristic mixing layer width l_m is small compared to the Kolmogorov scale η_k, there exists a laminar sublayer which is governed by molecular diffusion. In fact, the width of the mixing layer is small very close to the nozzle and broadens with increasing nozzle distance, which would correspond to the experimental findings. The transition to unity Lewis numbers would then occur when the mixing layer width becomes larger than the Kolmogorov scale and the turbulent eddies contribute to the transport within the mixing layer. Note that this does not violate the flamelet assumption, because the small turbulent scales, which can disturb the laminar structure of the mixing layer, can still be much larger than the reaction zone thickness, which is thin compared to the mixing layer.

For a rough estimate of the mixing layer thickness l_m, this can be determined as a characteristic length scale related to the maximum scalar dissipation rate as

$$l_m = \sqrt{\frac{2D_Z}{\chi_{\max}}} \, \Delta Z. \qquad (25)$$

This length scale is illustrated in the mixture fraction profile of a counterflow diffusion flame in Fig. 5. The value of $D_Z/\chi_{\max}$ has to be evaluated at the location of the maximum scalar dissipation rate, but can be related to stoichiometric conditions as

$$\left. \frac{D_Z}{\chi} \right|_{Z(\chi_{\max})} = c_{\mathrm{st}} \left. \frac{D_Z}{\chi} \right|_{Z_{\mathrm{st}}}, \qquad (26)$$

where the constant c_{st} can be estimated using Eq. 8 and $\lambda/c_p \sim T^{0.7}$ [31] to be approximately $c_{\mathrm{st}} \approx 0.1$ for the present case.

If the characteristic length and velocity scales of the large turbulent eddies and a characteristic mixture fraction fluctuation are defined by

$$l_t = \frac{\tilde{k}^{3/2}}{\tilde{\epsilon}}, \qquad u'' = \tilde{k}^{1/2}, \quad \text{and} \quad Z'' = \widetilde{Z''^2}^{1/2}, \qquad (27)$$

according to Eq. 12 the stoichiometric scalar dissipation rate can be estimated as

$$\chi_{\mathrm{st}} = \left(c_\chi \frac{u''}{l_t} Z''^{1/2} \right)_{\mathrm{st}}. \qquad (28)$$

The ratio of the mixing layer thickness and the length scale of the large turbulent eddies can then be expressed as

$$\frac{l_m}{l_t} = \frac{\Delta Z}{Z''} \sqrt{\frac{2c_{\mathrm{st}}}{c_\chi \mathrm{Sc}}} \, \mathrm{Re}_t^{-1/2}, \qquad (29)$$

where the molecular Schmidt number Sc is defined in accordance to Eq. 23 and the turbulence Reynolds number will be defined in Eq. 31.

With the Kolmogorov length scale given by

$$\eta_k = \left(\frac{\nu^3}{\tilde{\epsilon}} \right)^{1/4} \qquad (30)$$

the ratio of the length scales l_t and η_k can be written in terms of the turbulence Reynolds number Re_t as

$$\frac{l_t}{\eta_k} = \left(\frac{u'' l_t}{\nu} \right)^{3/4} = \mathrm{Re}_t^{3/4}. \qquad (31)$$

Introducing this in Eq. 29 yields the ratio of the mixing layer thickness and the Kolmogorov scale as

$$\frac{l_m}{\eta_k} = \frac{\Delta Z}{Z''} \sqrt{\frac{2c_{\mathrm{st}}}{c_\chi \mathrm{Sc}}} \, \mathrm{Re}_t^{1/4}. \qquad (32)$$

Following the arguments given earlier, differential diffusion effects should become important when the ratio $l_m/\eta_k < 1$. Equation 32 indeed reveals the experimentally found Reynolds number dependence that l_m/η_k tends to infinity for high Reynolds numbers, and becomes small at low Reynolds numbers. How-
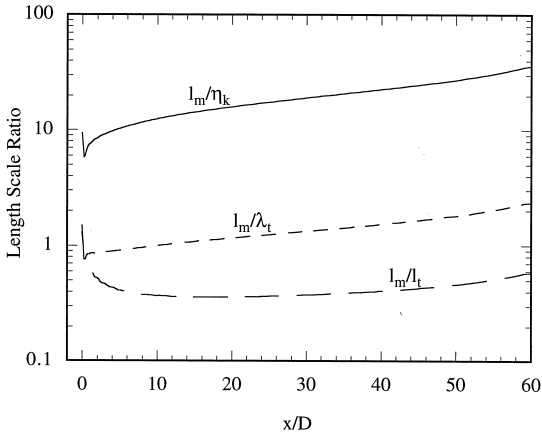
Fig. 6. Comparison of different length scale ratios along the contour of stoichiometric mixture.

ever, evaluating Eq. 32 along the contour of stoichiometric mixture for the investigated flame and $\Delta Z = 1$, which is suggested by the interpretation of l_m shown in Fig. 5, reveals that l_m/η_k is always much larger than unity, except for a region very close to the nozzle, where the difference in both length scales is less than an order of magnitude. This is shown in Fig. 6, where l_m/η_k is shown as a function of the nozzle distance.

It could also be argued that even if the ratio l_m/η_k is larger than one, the Kolmogorov eddies cannot contribute to the transport within the mixing layer because of the low energy per unit volume. Then, a larger length scale would be responsible for the transition from molecular to turbulent mixing. To demonstrate the impact of this assumption, Fig. 6 also presents l_m/l_t, and the ratio of the mixing layer thickness and the Taylor scale λ_t defined by

$$\lambda_t = \left(\frac{15 \nu \tilde{k}}{\tilde{\epsilon}} \right)^{1/2}, \qquad (33)$$

indicating that the large eddy length scale is always in the order of the mixing layer thickness. The Taylor length scale is indeed larger than l_m close to the nozzle, but the ratio becomes larger than one farther downstream.

Concludingly, it can be noted that the last two possible explanations for differential diffusion effects arising in turbulent flows given in this section could account for the occurrence of differential diffusion very close to the nozzle.

However, both rely on arguments based on the turbulence and it has been shown that there exists a laminar mixing layer in the near field of the nozzle in turbulent jet diffusion flames. It is therefore proposed that the occurrence of differential diffusion in the investigated turbulent jet flame is only caused by the existence of this laminar region. Some evidence for this will be given in the following section.

RESULTS AND DISCUSSION

In this section the results of the numerical simulations will be presented and compared to experimental data. First, the results of the flow field variables and species mass fractions are shown. Then, for a discussion of the remaining differences between measured and calculated data, the impact of the particular choice of the chemical mechanism and the influence of differential diffusion will be demonstrated.

Flow Field and Flame Structure

In the following, numerical results are mainly shown along the centerline and for radial slices at $x/D = 40$. The experimental data for temperature and species mass fractions have been taken from Bergmann et al. [5]. The species mass fractions have been determined by single-point Raman measurements, and the temperature by single-point Raman and Rayleigh measurements. The results of both techniques have been shown to be in good agreement. The uncertainties are estimated to be lower than 5% for the temperature and less than 10% for all species mass fractions except for CO, where because of the low concentrations in the jet flame, the error can be as high as 30–50%. The velocity measurements have been carried out by Hassel et al. [13] using laser Doppler velocimetry.

The combustion model described in this paper requires the calculation of laminar flamelets. The solution of these is completely coupled with the flow field solution. However, only little information, namely the axial velocity at stoichiometric mixture, the mean mixture fraction, and the variance of the mixture fraction is needed from the flow field solution for solving the
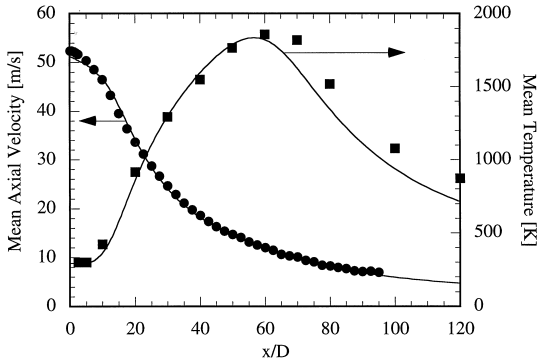
Fig. 7. Comparison of calculated (lines) mean axial velocity and mean temperature with experimental data (symbols) from Refs. 5 and 13 along the centerline.
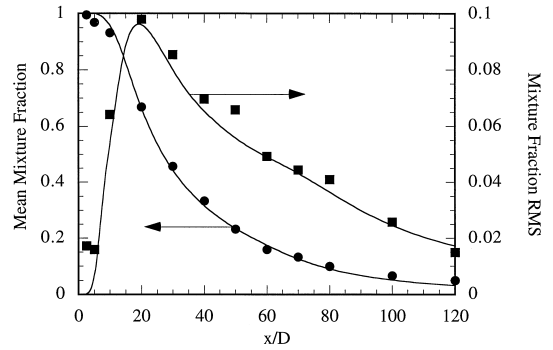

Fig. 9. Comparison of calculated (lines) mean and RMS of mixture fraction with experimental data (symbols) from Ref. 5 along the centerline.

laminar flamelet. Only if these data, which are an input rather than an output of the combustion model, are well predicted by the flow field solver, can the combustion model be expected to yield reasonable results. Therefore, the numerical solution for these quantities should be compared to the experimental data first.

The calculated turbulent mean values of the axial velocity are compared to the experimental data along the centerline in Fig. 7 and for a radial slice at $x/D = 40$ in Fig. 8. The velocity is predicted very well. The radial profile also shows that the spreading rate is calculated quite accurately. The axial development and the radial profile of the mean and the root mean square (RMS) of the mixture fraction are given in Figs. 9 and 10. Both the mean mixture fraction and its RMS are predicted excellently along the centerline. Downstream of $x/D = 60$,

the mean mixture fraction is slightly underpredicted, which will be discussed later. In the radial profiles, the mean mixture fraction seems to be overpredicted in the lean part of the flame and the calculated maximum value of the variance is approximately 35% too high.

This shows that the present test case, and in particular the comparison along the centerline, is very suitable to validate the combustion model, because the required data seem to be predicted very reasonably. The following discussion of the model predictions focuses therefore mainly on the centerline results. The errors caused by the wrongly predicted radial mixture fraction profile are minimized by presenting the radial data as a function of the mean mixture fraction. To elucidate the differences in these representations, some axial profiles are exemplarily given also as a function of the mean mixture fraction in Fig. 11 and the radial tem-
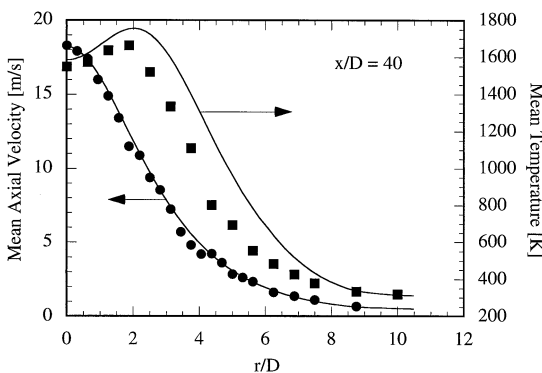

Fig. 8. Comparison of calculated (lines) mean axial velocity and mean temperature with experimental data (symbols) from Refs. 5 and 13 at $x/D = 40$.
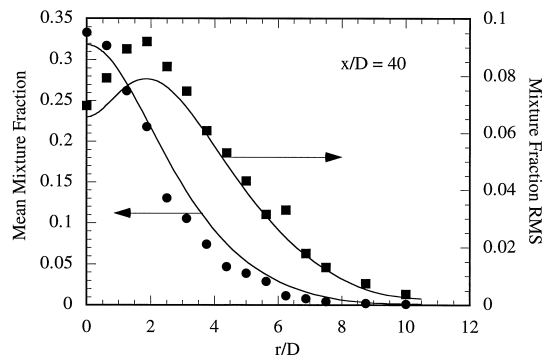

Fig. 10. Comparison of calculated (lines) mean and RMS of mixture fraction with experimental data (symbols) from Ref. 5 at $x/D = 40$.
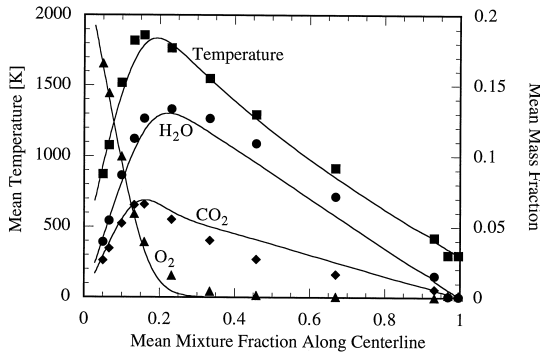
Fig. 11. Comparison of calculated (lines) mean temperature and mean mass fractions of O_2, H_2O, and CO_2 as a function of mean mixture fraction with experimental data (symbols) from Ref. 5 along the centerline.

Fig. 12. Comparison of calculated (lines) mean temperature and mean mass fractions of CH_4, H_2, and O_2 as a function of mean mixture fraction with experimental data (symbols) from Ref. 5 at $x/D = 40$.

perature profile is shown as a function of the physical coordinate in Fig. 8.

The mean temperature as a function of the nozzle distance is shown in Fig. 7. The agreement in the rich part is quite good. Farther downstream at approximately $x/D = 60$, when the centerline mixture fraction becomes smaller than its stoichiometric value, the temperature is underpredicted by approximately 150 K. However, this large discrepancy arises in part from a slight underprediction of the mixture fraction, which because of the large gradients in the lean part of the flamelet solution can have a strong influence on the predicted results. If the axial temperature development is compared to the experimental data as a function of the mean mixture fraction as shown in Fig. 11, the agreement seems to be improved. However, a slightly lower maximum temperature and a shift to the rich is still observable in the numerical results. This will be discussed below. Similar tendencies can be obtained in the radial temperature data shown in Fig. 8. In the outer, lean part of the jet, the temperature is overpredicted by approximately 200 K. However, this discrepancy can mainly be attributed to the wrongly predicted mean mixture fraction, which is demonstrated in Fig. 12, where the radial temperature profile is plotted over the mean mixture fraction, and as a result the remaining error is much smaller.

Mean mass fractions of molecular oxygen and the fuel components methane and molecular hydrogen are compared to experimental data along the axis of symmetry in Fig. 13 and in a
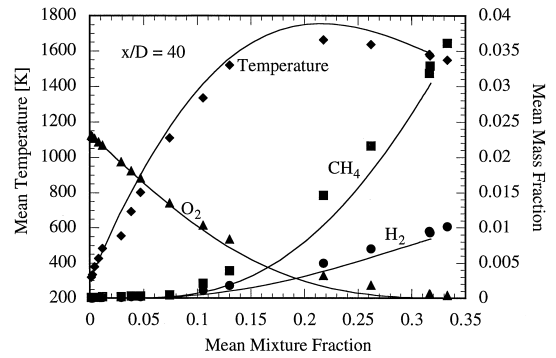
radial slice at $x/D = 40$ as a function of the mean mixture fraction in Fig. 12. The agreement, particularly for the centerline data, is very good. Again, the agreement in the lean part of the axial data is significantly improved by plotting as a function of the mean mixture fraction as shown in Fig. 11 for the O_2 mass fraction.

The intermediate species CO and the products H_2O and CO_2 are compared to the experimental data in Figs. 14 and 15. Especially the H_2O mass fraction is predicted quite well, although the experimental data are underpredicted in the lean part of the flame. If the large experimental uncertainty for the CO mass fraction of up to 50% is considered, then also CO can be regarded as sufficiently well described.
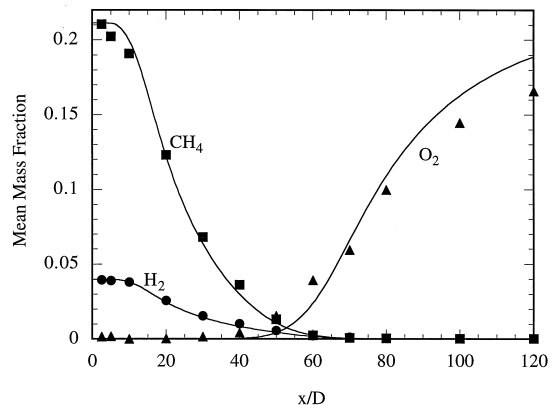

Fig. 13. Comparison of calculated (lines) mean mass fractions of CH_4, H_2, and O_2 with experimental data (symbols) from Ref. 5 along the centerline.
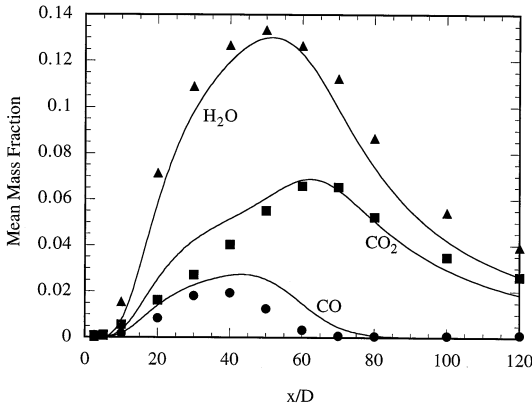
Fig. 14. Comparison of calculated (lines) mean mass fractions of CO, CO_2, and H_2O with experimental data (symbols) from Ref. 5 along the centerline.

Fig. 16. Comparison of calculated (lines) mean temperature and mean mass fractions of CH_4 with experimental data (symbols) from Ref. 5 along the centerline using three different chemical reaction mechanisms.

The CO_2 mass fraction is overpredicted by up to 50% in the region $20 < x/D < 40$.

Certainly, the discrepancies shown here are not distinct enough for an unambiguous error analysis. However, for an interpretation of the remaining errors, the sensitivity of the results regarding the chemical mechanism and the consideration of differential diffusion will be investigated in the following.

Chemical Mechanism

As described earlier, a reduced 20-step mechanism based on the detailed kinetic scheme by Warnatz et al. [25] has been used for the 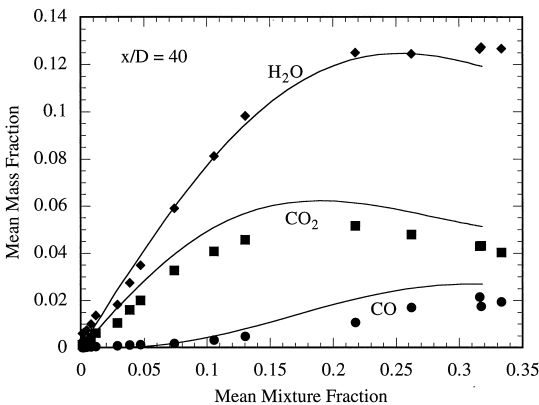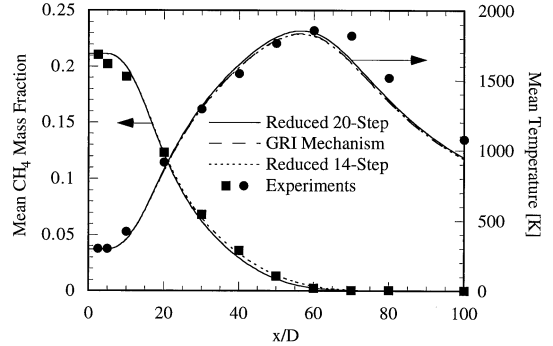calculations of the results presented in the previous section. The influence of the applied chemical mechanism has been investigated by performing additional calculations using the GRI-mechanism by Bowman et al. [32] consisting of 354 reactions among 30 species and a reduced 14-step mechanism based on a skeletal mechanism given by Peters [33].

Figure 16 shows the numerical results for the temperature and the CH_4 mass fraction using the three different mechanisms. The results can hardly be distinguished, indicating that fuel consumption and heat release are described very similarly by these kinetic schemes. Also for the H_2 and H_2O mass fractions, which are not shown, all mechanisms lead to almost identical results. However, as shown in Fig. 17 for the CO and CO_2 mass fractions, the results from the

Fig. 15. Comparison of calculated (lines) mean mass fractions of CO, CO_2, and H_2O as a function of mean mixture fraction with experimental data (symbols) from Ref. 5 at $x/D = 40$.
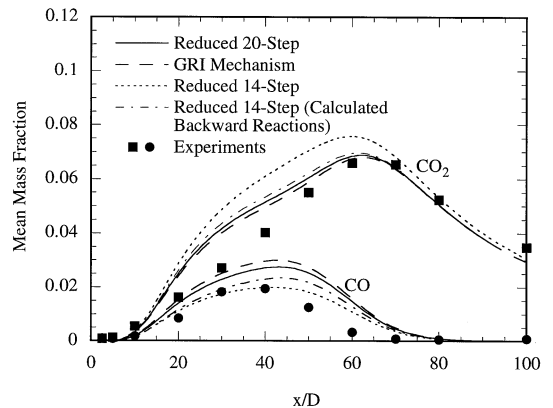

Fig. 17. Comparison of calculated (lines) mean temperature and mean mass fractions of CO and CO_2 with experimental data (symbols) from Ref. 5 along the centerline using three different chemical reaction mechanisms.

14-step mechanism depart from those of the 20-step Warnatz mechanism and the GRI mechanism, especially in the rich part of the flame, which extends from the nozzle to approximately $x/D = 60$. Both, Warnatz' mechanism and the GRI mechanism seem to yield much more accurate CO_2 mass fractions. However, in Ref. 33 kinetic rate data for the considered backward reactions are given explicitly. If those are computed from the equilibrium constants, the results of the 14-step mechanism are also very comparable to the other schemes. The CO mass fraction seems to be improved by the results of the 14-step mechanism. But since the experimental uncertainty for CO is very high, the results of all mechanisms are still in the bounds of the experimental error.

Differential Diffusion

The experimental data obtained by Bergmann et al. [5] clearly reveal differential diffusion effects close to the nozzle. These become weaker with increasing nozzle distance, but can still be observed at $x/D = 20$. In an earlier section it has been concluded that differential diffusion in the investigated jet flame is only caused by the existence of a laminar region close to the nozzle. This postulation should be confirmed and investigated further in the following.

In the context of differential diffusion it is important to clarify the applied definition of the mixture fraction. In the frame of the flamelet model as given in Ref. 15 the mixture fraction is defined by the solution of a conservation equation as given by Eq. 1. This definition is used for all calculations in the present paper. Because a mixture fraction defined as such cannot be obtained from the experimental data, an element mixture fraction based definition, as for example given by Masri and Bilger [16], has to be used in order to compare the numerical results with the experiments. However, the turbulent mean of this mixture fraction definition can be determined from flow field and flamelet solution very easily and is therefore applied in the comparisons with experimental data in this section. As mentioned earlier, for the equal Lewis number approach there is no difference between both definitions.
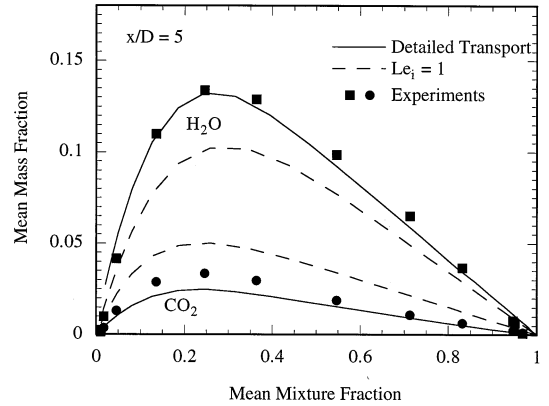

Fig. 18. Comparison of calculation considering differential diffusion with calculation assuming unity Lewis numbers and experimental data from Ref. 5 at $x/D = 5$.

To demonstrate the fundamental influence of nonunity Lewis numbers, numerical simulations have been performed using the Lagrangian Flamelet Model with a recently developed flamelet formulation that can account for differential diffusion effects [15]. The results of the detailed molecular transport calculations are compared to the results of the previous section, where unity Lewis numbers for all chemical species have been assumed, and to experimental data in Figs. 18 and 19. Figure 18 shows the radial distribution of H_2O and CO_2 at a nozzle distance of $x/D = 5$. At this location the maximum H_2O mass fraction is underpredicted, whereas the predicted CO_2 mass fraction is too high, if unity Lewis numbers are assumed for all chemical species. However, if differential diffu-
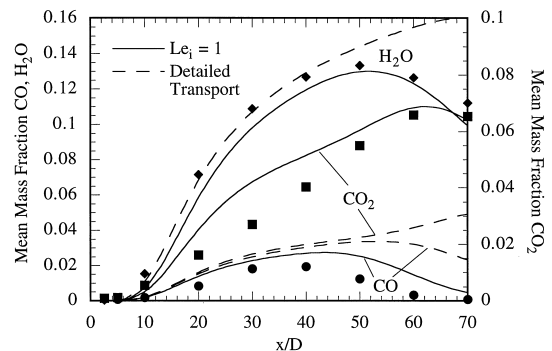

Fig. 19. Comparison of calculation considering differential diffusion with calculation assuming unity Lewis numbers and experimental data from Ref. 5 along the centerline.

sion is considered, both H_2O and CO_2 mass fractions are significantly improved.

In Fig. 19 a comparison of the detailed transport calculations with the unity Lewis number results and the experimental data for H_2O, CO, and CO_2 is given along the axis of symmetry. Again, the results for H_2O are improved close to the nozzle by considering differential diffusion. Also for the CO_2 mass fraction, the consideration of differential diffusion yields the right tendency, but the correction is too strong, leading to an underprediction of the CO_2 mass fraction. The CO profile is hardly influenced by differential diffusion in the region close to the nozzle. However, downstream of $x/D \approx 40$ the results of the differential diffusion calculations depart clearly from the experimental data for the mass fractions of all three components, whereas the results obtained using the unity Lewis number approach match the experimental data quite well. These results seem to confirm the experimental findings that differential diffusion is most important in the nozzle close region.

In order to validate the suggested model, an additional calculation has been performed using the flamelet equations given in Ref. 15. For this calculation it has been assumed that as long as the jet reveals a potential core, there is no turbulent diffusion of chemical species occurring within the mixing layer.

For this assumption the application of the standard $\bar{k} - \bar{\epsilon}$ model causes two problems. Firstly, this model cannot account for the laminar mixing layer region close to the nozzle. However, it has been shown that the velocity and also the mixture fraction field are well predicted. With respect to the scalar dissipation rate, recent work presenting $\bar{k} - \bar{\epsilon}$ model and large-eddy simulation calculations for the same jet diffusion flame [34, 35] indicates that the predictions for the scalar dissipation rate are not very different even in the region close to the nozzle. The second problem is that the transition point cannot be determined by the use of the $\bar{k} - \bar{\epsilon}$ model. Because it is not the intention of the present model to predict the transition point, this value will be prescribed by the examination of the experimental data for the present study. However, both problems can probably be cured by the use of large-eddy simulations.

From Fig. 3 the potential core region can be estimated to extend from the nozzle to approximately $x/D = 10$. At this point, the laminar–turbulent transition is assumed to occur and the calculation of the unsteady flamelet continues downstream with unity Lewis numbers for all species. This choice seems to be somewhat arbitrary, but it is strongly supported by element mass fraction distributions discussed later in this paper, which clearly show molecular transport being dominant up to a nozzle distance of $x/D = 10$. For the assumption of $Le_i = 1$, it can be shown easily that the flamelet equations given in Ref. 15 simplify to Eqs. 4 and 5.

The results along the centerline are compared to the experimental data for the temperature as well as H_2O and CO_2 mass fractions in Fig. 20. In addition, the results assuming unity Lewis numbers throughout the whole calculation are given in this figure. The consideration of differential diffusion in the laminar region close to the nozzle improves the CO_2 and the H_2O mass fractions in the upstream part of the flame. Interestingly, also in the downstream lean part, the calculated temperature and the H_2O mass fraction are in significantly better agreement with the experiments. The CO mass fraction is hardly influenced by the consideration of differential diffusion and the presentation has therefore been omitted.

Although in the calculations the Lewis numbers are different from unity only very close to the nozzle exit, Fig. 20 shows clearly that also the downstream region is obviously influenced by differential diffusion effects and the results do not approach the equal diffusivity solution within the computational domain. A further investigation shows that after the transition, when the Lewis numbers for all components are changed to unity, the initial mixing state, which is strongly influenced by the consideration of differential diffusion in the region close to the nozzle, does not disappear immediately. When the turbulent mixing proceeds, the scalar dissipation rate decreases strongly and this mixing state becomes frozen.

This is demonstrated in Fig. 21, where the computed conditional mean H atom mixture fraction Z_H is given as a function of the conditional mean C atom mixture fraction Z_C. For a comparison with the experiments, the condi-
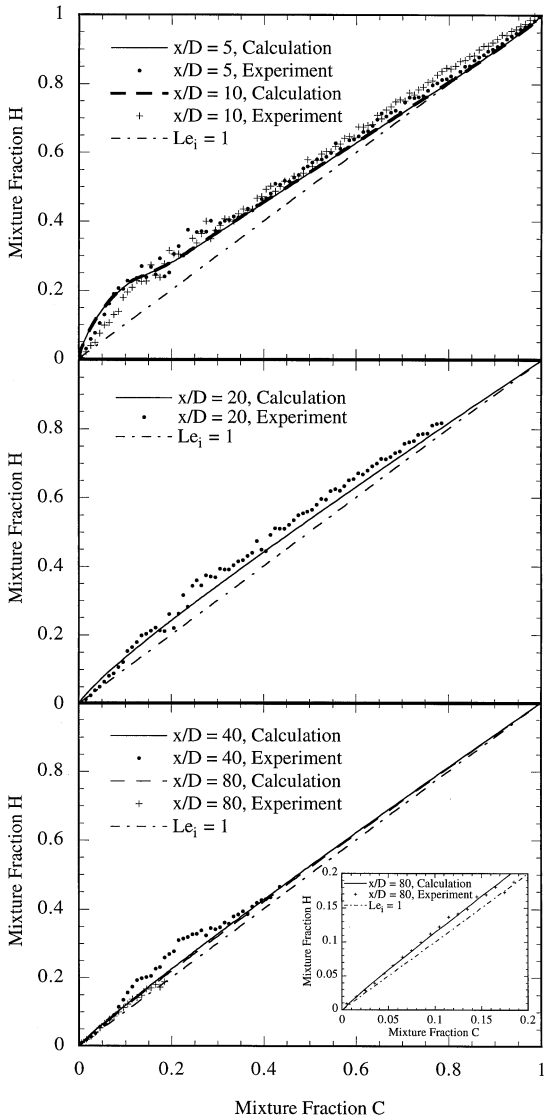
Fig. 20. H atom mixture fraction as a function of C atom mixture fraction from calculation considering differential diffusion for $x/D < 10$ and assuming unity Lewis numbers downstream compared to unity Lewis number approach and experimental data from Ref. 5 along the centerline.
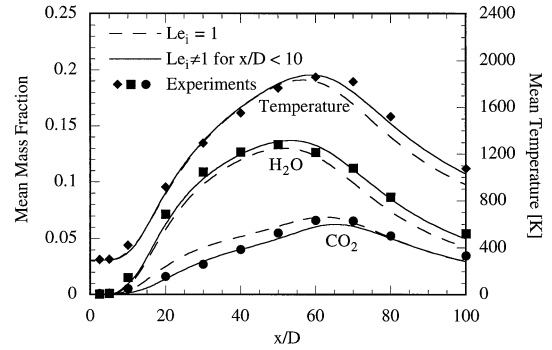

Fig. 21. Comparison of calculation considering differential diffusion for $x/D < 10$ and assuming unity Lewis numbers downstream with calculation assuming unity Lewis numbers and experimental data from Ref. 5 along the centerline.

At $x/D = 5$ and $x/D = 10$, the influence of differential diffusion is very strong because the flow is assumed to be laminar. This assumption is confirmed by the experimental data, which match the calculations at these points quite well. Both the calculated and the experimental data at the two locations can hardly be distinguished, indicating that the data are not affected by turbulent transport, and that molecular diffusion is predominant. At $x/D = 10$, the laminar–turbulent transition is assumed to occur and all Lewis numbers are assumed to be unity. In the downstream calculation, the element mixture fractions approach the straight line of the equal diffusivity results. At $x/D = 20$, the differential diffusion effects have become much weaker, which is also reflected by the experimental data. At $x/D = 40$, the computed results are quite close to the unity Lewis number solution. However, at this point the differential diffusion influenced mixing state becomes frozen and remains almost unchanged until $x/D = 80$. The experimental data at $x/D = 40$ is still slightly higher than the model predictions, but at $x/D = 80$ the data agree well with the model, showing the H atom mixture fraction to be approximately 15% higher than for the $Le_i = 1$ case. The possibility that the deviation from the equal diffusivity line originates merely from experimental uncertainties can be precluded, because this effect has not been observed in similar experiments in natural gas flames, where differential diffusion is not expected to be of importance [36].

tional mean element mixture fractions have been evaluated from single-pulse data obtained by Bergmann et al. [5] using a bin size of $\Delta Z_B = 0.01$ for conditioning on the mixture fraction. All bins with fewer than 10 samples have been disregarded. In the case of unity Lewis numbers, the element mixture fractions Z_C and Z_H have the same steady solution and the function $Z_H(Z_C)$ is given by a straight line with a slope of unity, which is also depicted in Fig. 21.

CONCLUSIONS

In the present paper it has been shown that the computational results applying the unsteady flamelet model for a nonpremixed, steady, turbulent $CH_4/H_2/N_2$–air diffusion flame are in good agreement with experiments for axial velocity, mixture fraction, species mass fractions, and temperature.

Differential diffusion effects, which can clearly be observed in the experimental data throughout the whole flame, have been shown to arise from the existence of a laminar region very close to the nozzle. In this region, which is governed by molecular diffusion, because of nonequal diffusivities, a mixing state strongly influenced by differential diffusion is established. After transition to a turbulent flow, which is assumed to occur at the end of the potential core, the element distribution approaches the equal diffusivity solution. However, because of the rapid decrease of the scalar dissipation rate, this mixing state becomes frozen before the equal diffusivity distribution is achieved. Hence, the temperature and the species mass fractions are influenced by differential diffusion even far downstream of the nozzle.

As a consequence, differential diffusion appears after the end of the potential core of the jet only as an unsteady effect that can be described by a unity Lewis number unsteady flamelet model. Steady flamelet library models are therefore inherently unsuitable to describe these phenomena. For the laminar region close to the nozzle, a previously developed flamelet formulation capable of describing differential diffusion can be used.

The proposed mechanism leading to differential diffusion in the investigated flame configuration fulfills several requirements, which are known from experimental observations. For instance, it can be shown that the model predicts the equal diffusivity solution for infinite distance from the nozzle or infinite Reynolds number.

Although it cannot be shown in the frame of this work, it seems to be very probable that the proposed mechanism is the main source for differential diffusion effects for jet flames with Reynolds numbers clearly above transition. This implies that models that are intended to be capable of predicting differential diffusion effects in jet flames have to take the laminar region close to the nozzle into consideration.

The extent of the laminar region has in the present paper been prescribed from the experimental data. The determination of this has to be included in the calculations by the use of more elaborate turbulence models such as large-eddy simulations.

REFERENCES

1. Pitsch, H., Chen, M., and Peters, N., *Proceedings of the Combustion Institute, vol. 27*, The Combustion Institute, Pittsburgh, 1998, pp. 1057–1064.
2. Drake, M. C., Lapp, M., Penney, C. M., Warshaw, S., and Gerhold, B. W., *Proceedings of the Combustion Institute, vol. 18*, The Combustion Institute, Pittsburgh, 1981, p. 1521.
3. Barlow, R. S., and Frank, J. H., Poster W2E07, presented at the Third International Workshop on Measurement and Computation of Turbulent Nonpremixed Flames, Boulder, Colorado, 1998, http://www.ca.sandia.gov/tdf/3rdWorkshop/Boulder.html.
4. Drake, M. C., Pitz, R. W., and Lapp, M., *AIAA J.* 24:905 (1986).
5. Bergmann, V., Meier, W., Wolff, D., and Stricker, W., *Appl. Phys. B* 66:489–502 (1998).
6. Meier, W., Prucker, S., Cao, M.-H., and Stricker, W., *Combust. Sci. Technol.* 118:293 (1996).
7. Yeung, P. K., and Pope, S. B., *Phys. Fluids A* 5:2467 (1993).
8. Nilsen, V., and Kosály, G., *Phys. Fluids* 9:3386 (1997).
9. Kronenburg, A., and Bilger, R. W., *Phys. Fluids* 9:1435 (1997).
10. Nilsen, V., and Kosály, G., *Combust. Flame*, 117:493–513, 1999.
11. Bilger, R. W., *AIAA J.* 20:962–970 (1982).
12. Chen, J.-Y., and Chang, W.-C., *Combust. Sci. Technol.*, 133:343–375, 1998.
13. Hassel, E., Geiß, S., http://www.tu-darmstadt.de/fb/mb/ekt/flamebase.html, 1998.
14. Pope, S. B., *AIAA J.* 16:279 (1978).
15. Pitsch, H., and Peters, N., *Combust. Flame* 114:26–40 (1998).
16. Masri, A. R., and Bilger, R. W., *Combust. Flame* 73:261–285 (1988).
17. Peters, N., *Prog. Energy Combust. Sci.* 10:319 (1984).
18. Peters, N., *Proceedings of the Combustion Institute, vol. 21*, The Combustion Institute, Pittsburgh, 1986, p. 1231.
19. Pitsch, H., Wan, Y. P., and Peters, N., SAE Paper 952357, 1995.
20. Pitsch, H., Barths, H., and Peters, N., SAE Paper 962057, 1996.

21. Jones, W. P., and Whitelaw, J. H., *Combust. Flame* 48:1 (1982).

22. Maz'ja, V. G., *Sobelev Spaces*, Springer Verlag, Berlin, 1985, p. 37.

23. Kollmann, W., and Chen, J. H., *Proceedings of the Combustion Institute, vol. 21*, The Combustion Institute, Pittsburgh, 1994, pp. 777–784.

24. O'Brien, E. E., in *Turbulent Reacting Flows* (P. A. Libby and F. A. Williams, Eds.), Springer, 1980.

25. Warnatz, J., Maas, U., and Dibble, R. W., *Combustion, Physical and Chemical Fundamentals, Modeling and Simulation, Experiments, Pollutant Formation*, Springer Verlag, 1996.

26. Yule, A. J., Chigier, N. A., Ralph, S., Boulderstone, R., and Ventura, J., *AIAA J.* 19:752–760 (1980).

27. Schefer, R. W., Namazian, M., Filtopoulos, E. E. J., and Kelly, J., *Proceedings of the Combustion Institute, vol. 25*, The Combustion Institute, Pittsburgh, 1994, pp. 1223–1231.

28. Chen, L.-D., Roquemore, W. M., Goss, L. P., and Vilimpoc, V., *Combust. Sci. Technol.* 77:41–57 (1991).

29. Clemens, N. T., and Paul, P. H., *Combust. Flame* 102:271–284 (1995).

30. Soteriou, M. C., *Proceedings of the Combustion Institute, vol. 27*, The Combustion Institute, pp. 1213–1219 Pittsburgh, 1998.

31. Smooke, M. D., and Giovangigli, V., in *Reduced Kinetic Mechanisms and Asymptotic Approximations for Methane–Air Flames* (M. D. Smooke, Ed.), Springer, 1991.

32. Bowman, C. T., Hanson, R. K., Davidson, D. F., Gardiner, Jr., W. C., Lissianski, V., Smith, G. P., Golden, D. M., Frenklach, M., and Goldenberg, M., http://www.me.berkeley.edu/gri_mech/

33. Peters, N., in *Reduced Kinetic Mechanisms for Applications in Combustion Systems* (Peters and Rogg, Eds.), Springer, 1993. Springer Verlag, Berlin (Peters, N. and Rogg, B., Eds.)

34. Pitsch, H., and Riesmeier, E., Poster presented at the Fourth International Workshop on Measurement and Computation of Turbulent Nonpremixed Flames, Darmstadt, 1999.

35. Pitsch, H., and Steiner, H., Poster presented at the Fourth International Workshop on Measurement and Computation of Turbulent Nonpremixed Flames, Darmstadt, 1999.

36. Meier, W., Private communication, 1999.